Received 14 August 2023; revised 13 November 2023 and 5 December 2023; accepted 9 December 2023. Date of publication 13 December 2023; date of current version 29 January 2024. The review of this article was arranged by Editor G. I. Ng.

Digital Object Identifier 10.1109/JEDS.2023.3342469

The Dual-Mode Integration of Power Amplifier and Radio Frequency Switch Based on GaN Dual-Gate HEMTs

MENG ZHANG[1], HAOZHENG WANG[2], LING YANG[1] (Member, IEEE), BIN HOU[1], MEI WU[1] (Member, IEEE), QING ZHU[1], MINHAN MI[1], XU ZOU[1], CHUNZHOU SHI[2], QIAN YU[1], WENLIANG LIU[1], HAO LU[1] (Member, IEEE), XIAOHUA MA[1] (Member, IEEE), AND YUE HAO[1] (Senior Member, IEEE)

1 State Key Discipline Laboratory of Wide Band-Gap Semiconductor Technology, School of Microelectronics, Xidian University, Xi'an 710071, China
2 State Key Discipline Laboratory of Wide Band-Gap Semiconductor Technology, School of Advanced Materials and Nanotechnology, Xidian University, Xi'an 710071, China

CORRESPONDING AUTHORS: L. YANG AND H. LU (e-mail: yangling@xidian.edu.cn; luhao@xidian.edu.cn)

This work was supported in part by the National Natural Science Foundation of China under Grant 62234009, Grant 62090014, Grant 62104179, Grant 62104178, Grant 62104184, Grant 62131014, and Grant 62188102; in part by the China National Postdoctoral Program for Innovative Talents under Grant BX20200262; in part by the Postdoctoral Fellowship Program of CPSF under Grant GZB20230557; in part by the China Postdoctoral Science Foundation under Grant 2021M692499, Grant 2022T150505, and Grant 2023M732730; and in part by the Fundamental Research Funds for the Central Universities of China under Grant XJSJ23056 and Grant ZDRC2002.

ABSTRACT In this paper, an integrated device which realized the dual-mode integration of power amplifier (PA) and radio frequency (RF) switch based on GaN dual-gate (DG) structure is designed and fabricated. The integrated device provides two working modes and meets the performance requirements of PA and RF switch. In the transmit (Tx) mode, the integrated device is used as PA. At the frequency of 3.6 GHz, compared with the conventional GaN HEMT (high electron mobility transistor) as PA, due to the field modulation effect of the dual-gate structure, the current collapse is effectively suppressed, and the output power density (P_{out}) of the integrated device is increased from 6.90 W/mm to 7.85 W/mm, and the power added efficiency (PAE) is increased from 44.3% to 51.1%. In the receive (Rx) mode, the integrated device is used as RF switch. Compared with conventional RF switch, the isolation of integrated devices is significantly improved. At the frequency of 3.6GHz, the isolation is improved from 19.4 dB to 41.0 dB; At the frequency of 40 GHz, the isolation is improved from 3.0 dB to 29.7 dB. The integrated device provides a novel function integration scheme for RF frontends, with great potential for improving the integration and dimension of future communication systems.

INDEX TERMS Gallium nitride, integrated device, power amplifier, RF switch, HEMT.

I. INTRODUCTION

With the rapid development of wireless communications and the appearance of phased array radars and massive MIMO, the RF frontends occupies an irreplaceable role in thewireless communication system [1], [2], [3]. The RF frontends is composed of a transmitter and a receiver. As show in Fig. 1(a), the power amplifiers (PA) and RF switch are key components in the transceiver system. High output power (P_{out}) and power added efficiency (PAE) are required for PA [4], [5], [6]. Low insertion loss (IL) and high isolation (ISO) are necessary for RF switch [7], [8], [9]. As the representative of the third-generation semiconductor material, Gallium Nitride (GaN) has many superior material properties, such as wide bandgap, high breakdown electric field, and high electron saturation speed. Therefore, GaN-based high electron mobility transistors (HEMTs) show great potential in the RF frontends due to low on-resistance and high breakdown voltage [10], [11], [12], [13], [14]. Moreover, GaN HEMTs are the promising candidate for RF switch application because of high power tolerance [15], [16], [17].

For conventional RF front, a basic unit of single-pole double-throw (SPDT) switch is needed to switch the mode

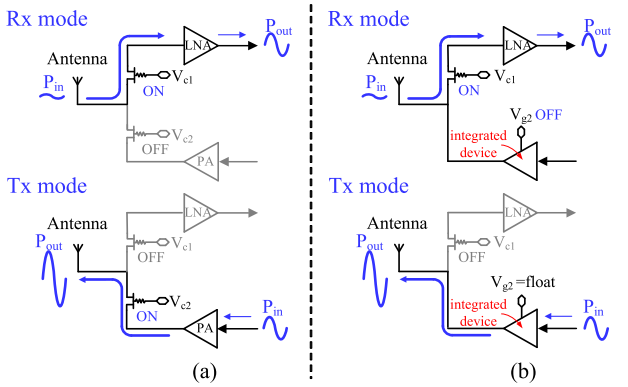

FIGURE 1. (a) Conventional Tx/Rx switching scheme. (b) Proposed Tx/Rx switching scheme.

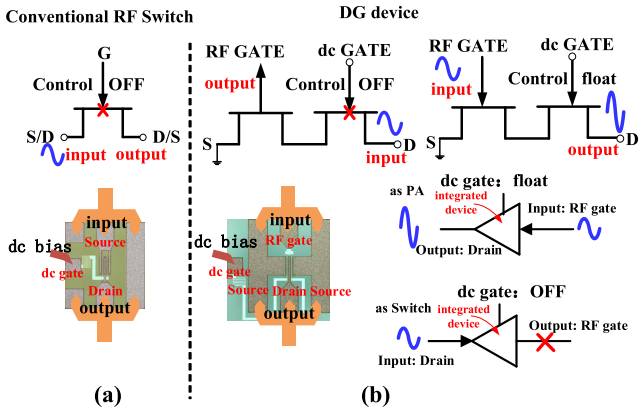

FIGURE 2. Comparison of working principle between (a) Conventional RF switch device and (b) DG device.

of transmit and receive. It is necessary to use several times of GaN-based HEMTs to construct SPDTs than that of PAs [18], [19], especially for the massive multiple-input multiple-output (MIMO) application, which will occupy a lot of chip area.

In this paper, we proposed a working principle based on AlGaN/GaN HEMT with dual-gate (DG) structure, which integrates the performance requirements of PA and RF switch. Different from GaN-based HEMTs with DG structure in early researches which primarily enhanced the device performance such as subthreshold swing, small signal gain and PAE for PA application [20], [21], [22], the RF switch application of the DG structure is extended in this paper with the proposed device working principle.

II. DEVICE STRUCTURE AND FABRICATION

Fig. 1(b) illustrates the working principle of the novel integrated device. In the Tx mode, the DG device exhibits the performance of the PA. In the Rx mode, the integrated device exhibits the performance of the RF switch. For conventional RF switch device, source/drain is used as the input/output of the signal, while for the DG device operated in the Rx mode, the signal inputs from the drain and is isolated by the control of dc gate which prevent the signal from outputting through the RF gate.

Fig. 2 shows a comparison of the operation principle of the conventional RF switch device and DG device. As shown in Fig. 2(a), for conventional RF switch, the signal is input from source/drain and output through drain/source. The channel is controlled by the gate to realize the on/off mode switching of the RF signal. For the on-wafer measurement, one end of the microwave probe is the source and the other end is the drain. The RF signal can be tested with a microwave probe, and the gate can be controlled by the direct current bias. As shown in Fig. 2(b), for the DG device operated in the Tx mode, the signal is input by the RF gate and output by the drain. The source is grounding, and the dc gate is not biased (floating), and the quiescent RF gate voltage and drain voltage is biased under class AB operation which ensures the power amplification of the signal. For the DG device operated in the Rx mode, the DG device insulates

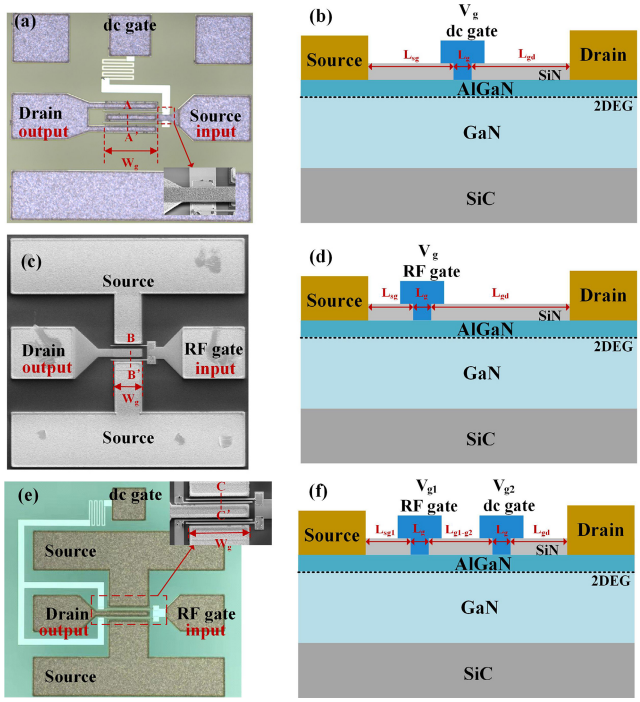

FIGURE 3. (a) The photograph and (b) schematic cross-section schematic along cutline AA′ for SG RF switch; (c) The photograph and (d) cross-section schematic along cutline BB′ for SG PA device; (e) The photograph and (f) cross-section schematic along cutline CC′ for DG device. The inset figure in Fig. 3(a) and (e) showed the enlarged photograph for the dashed rectangular region

the received signal by the off-state bias of the dc gate to switch off the channel. Due to the rectification effect of Schottky gate, the channel is pinched off and the input signal is blocked.

The structure diagram of the fabricated AlGaN/GaN HEMT is presented in Fig. 3(a). The un-doped AlGaN/GaN hetero-structure layers were grown on a 3-inch SiC substrate by metal organic chemical vapor deposition. The epitaxial layers consisted of 100-nm AlN nuclear layer, 800-nm GaN Fe-doped buffer, 400-nm unintentionally doped GaN buffer layer, 1-nm AlN layer, 20-nm undoped $Al_{0.25}Ga_{0.75}N$ barrier

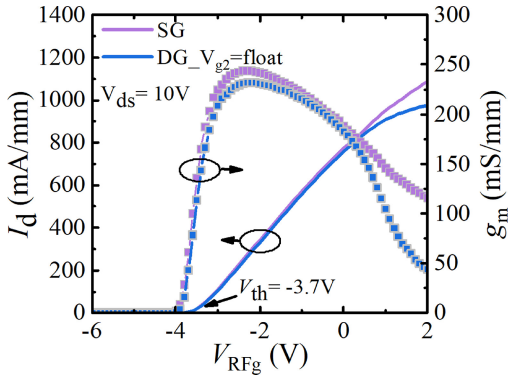

FIGURE 4. Comparison of transfer characteristic between SG device and DG device with dc gate floating.

layer, and 2.5-nm GaN cap layer from down to top. Room-temperature Hall measurement showed the 2DEG density of 9.92×10^{12} cm^{-2} and the electron mobility of 1853 cm^2/V·s. The device fabrication process began with the formation of ohmic contact. The Ti/Al/Ni/Au ohmic metal stack was evaporated followed with the rapid annealing at 850 °C for 30 s in N_2 atmosphere. The ohmic contact resistance (R_c) of 0.50 Ω·mm was measured using the transmission line measurement structure. Planar isolation was achieved by multi-energy N^+ implantations. Next, a 120-nm thick SiN passivation layer was deposited by plasma enhanced chemical vapor deposition (PECVD). Then, the gate foot was defined with the gate length (L_g) of 0.5 μm by lithography and CF_4-based plasma etching, followed by the deposition of Ni/Au gate metal stack to fabricate the T-shaped gate profile with gate head length of 1.3 μm. The geometry size of RF gate (V_{g1}) and dc gate (V_{g2}) for the integrated device was the same. In addition, a 10 kΩ NiCr thin-film resistor in series with the dc gate is prepared by sputtering in order to facilitate RF isolation, which is important for the protection of the RF front. Finally, Ti/Au metal stack was deposited to form the interconnection. Fig. 3(b) shows the top view photograph of the GaN-based integrated device. For comparison, we fabricated three different types of devices on the same wafer: conventional GaN HEMT as PA device (SG PA device), conventional GaN HEMT RF switch (SG RF switch) device and GaN based integrated device (DG device). The DG device has a source to the RF gate spacing (L_{sg1}) of 1.4 μm, RF gate to the dc gate spacing (L_{g1-g2}) of 2.0 μm and dc gate to the drain spacing (L_{g2d}) of 1.6 μm. The conventional GaN HEMT as PA device has a source to the gate spacing (L_{sg}) of 1.4 μm and gate to the drain spacing (L_{gd}) of 4.1 μm. The conventional GaN HEMTs RF switch device has the same geometry with the SG device. The gate width of the three kinds of devices is 200 μm.

III. DEVICE CHARACTERISTICS AND DISCUSSION

Fig. 4 shows the transfer characteristics of two kinds of devices with the gate width of 200 μm at V_{ds} = 10 V. The SG devices exhibited a maximum drain current density

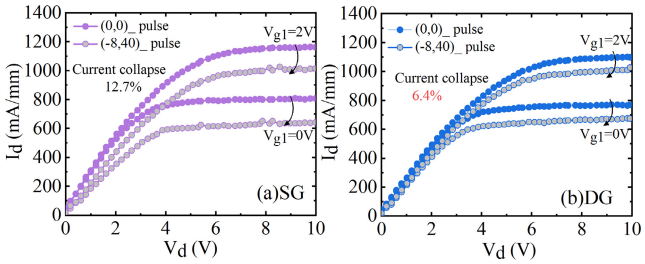

FIGURE 5. Pulsed output characteristics of (a) SG device and (b) DG device.

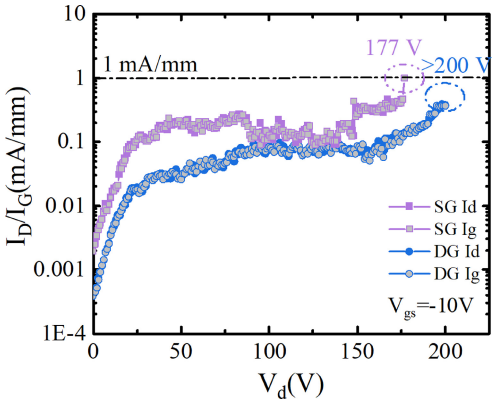

FIGURE 6. Three-terminal breakdown characteristics of SG device and DG device with the L_{sd} of 6 μm.

(I_{dmax}) of 1086 mA/mm and a peak transconductance (g_m) of 243.8 mS/mm. When the dc gate was not biased and at the floating state, the DG devices exhibited an I_{dmax} of 974 mA/mm and a peak g_m of 231.9 mS/mm. The threshold voltage (V_{th}) of both types of devices is −3.7 V. As shown in Fig. 4, when $V_g \leq 0$V for SG device and $V_{RFg} \leq 0$V for DG device, because the channel resistance under the RF gate region accounts for the majority in the channel resistance from source to drain, the influence of dc gate on I-V curve is not significant and the drain current density of SG device is a little more than that of DG device. When $V_g \geq 0$V for SG device and $V_{RFg} \geq 0$V for DG device, the channel resistance under the RF gate region reduces and the channel resistance under the dc gate region is comparable with the channel resistance under the RF gate region for DG device, leading to the reduction of drain current density compared with SG device.

Fig. 5(a) and Fig. 5(b) show the pulsed output characteristics of SG device and DG device. The pulse width and pulse period are 500ns and 1ms, respectively. The quiescent operating points (V_{gsq}, V_{dsq}) are (0V, 0V) and (−8V, 40V), respectively. As shown in Fig. 5, due to the field modulation of the dc gate, the DG device realizes the improvement of current collapse with collapse ratio of 6.4%, while the current collapse ratio of the SG device achieves 12.7%.

The OFF-state three-terminal breakdown characteristics of SG device and DG device at V_{GS} = −10 V were shown in Fig. 6. For both SG and DG device, during the breakdown

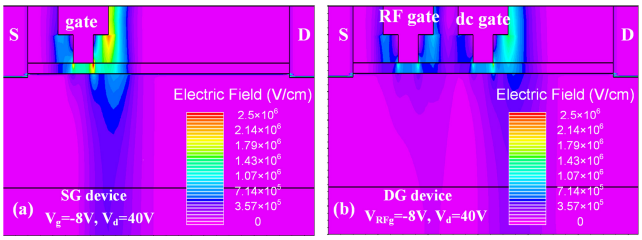

FIGURE 7. **The electric field distributions of (a) SG device and (b) DG device by ATLAS.**

measurement, the gate current was almost equal to the drain current, indicating the gate breakdown phenomenon. For DG device, V_{g2} was floating during the measurement. The breakdown voltage of SG device and DG device is 177 V and >200 V, respectively, with the breakdown standard of drain leakage current density of 1mA/mm. Due to the field modulation effect of the dc gate, the GaN-based DG device can effectively reduce the off-state leakage current and increase the breakdown voltage.

Fig. 7(a) and 7(b) show the electric field distributions of SG device and DG device at $V_{RFg} = -8$ V and $V_{ds} = 40$ V, respectively. For the electric field simulation, Fe-doping induced acceptor-like trap with energy level of E_c-0.57eV [23] and trap concentration of 1×10^{19} cm^{-3} was introduced in the GaN buffer layer. The dc gate at the floating state can reduce the electric field peak at the edge of the RF gate of the DG device compared to the SG device. The reduction of the electric field peak can effectively suppress the trap charging behavior and thus improved the current collapse [24], [25], [26], [27]. Moreover, the reduction of the peak value of electric field can also reduce the gate leakage, improve the current collapse and increase the breakdown voltage of DG devices.

The small signal characteristics of both devices were measured by Keysight E8363B network analyzer. The maximum current gain cutoff frequency (f_T) and the maximum power gain cutoff frequency (f_{max}) are obtained by extrapolating h_{21} and maximum stable power gain (MSG) with the slope of −20dB/decade. At $V_g = -2.5$ V and $V_{ds} = 10$ V, the SG device achieved f_T of 15.1 GHz and f_{MAX} of 36.4 GHz, while the DG device achieved f_T of 14.6 GHz and f_{MAX} of 36.6 GHz with the dc gate working in the floating state, as shown in Fig. 8. The decrease of f_T can be attributed to the reduction of the peak g_m.

The power measurement curves are shown in Fig. 9(a). The Maury load-pull system was used to perform the continuous wave RF power measurements at 3.6 GHz. The drain quiescent voltage (V_{DQ}) was biased at 50V. The RF gate was biased near the pinch-off voltage to ensure deep Class AB operation and the drain quiescent current (I_{DQ}) was set at 10% of the saturated drain current (I_{Dmax}). The power density was calculated as the output power divided by the total gate width. For equitable comparison, the gate width of dc gate in DG device was not included in the

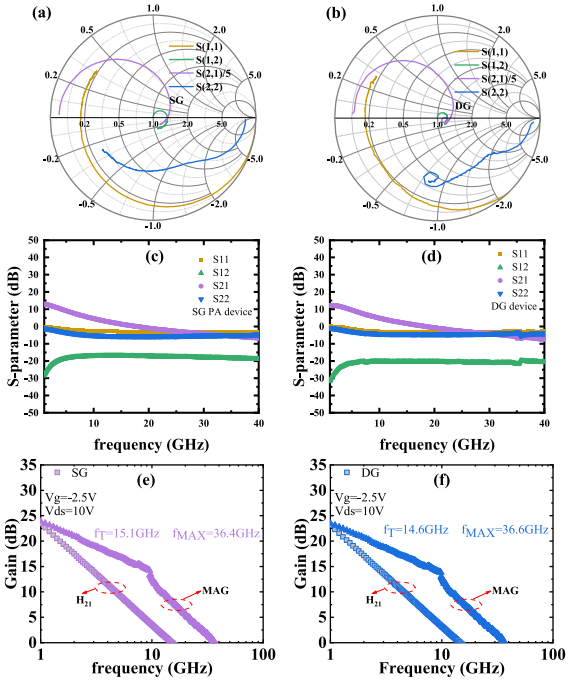

FIGURE 8. **Comparison of S parameters between (a)(c) SG device and (b)(d) DG device, and comparison of small signal characteristics of (e) SG device and (f) DG device.**

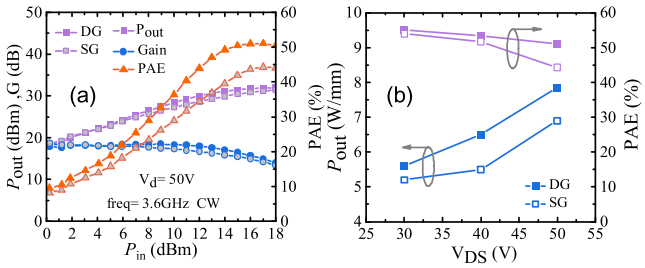

FIGURE 9. **(a) Power sweep measurements performed at 3.6 GHz. (b) P_{out} and PAE versus drain voltage in SG PA device and DG device.**

total gate width. The load and the source impedance were tuned for optimum PAE. The PAE and P_{out} of SG device were 44.3% and 6.90 W/mm, respectively, while that of DG device were 51.5% and 7.85 W/mm, respectively. The excellent power performance of DG device was attributed to the improved current collapse and the suppressed leakage current [25], [28]. In the future work, the PAE of DG device can be further increased by reducing the ohmic contact resistance [5], [29].

Fig. 9(b) shows the P_{out} and PAE of SG device and DG device as a function of drain voltage. In Fig. 9(b), V_{DQ} was biased at 30, 40 and 50V, respectively, and I_{DQ} was also set as 10% of I_{Dmax}, which means (I_{DQ}, V_{DQ}) = (21.7 mA, 30/40/50 V) for SG device and (I_{DQ}, V_{DQ}) = (19.4 mA, 30/40/50 V) for DG device. With the increase of drain voltage, the P_{out} of DG device increases more significantly than that of SG device, and the PAE of DG device decreases less than that of SG device. The main

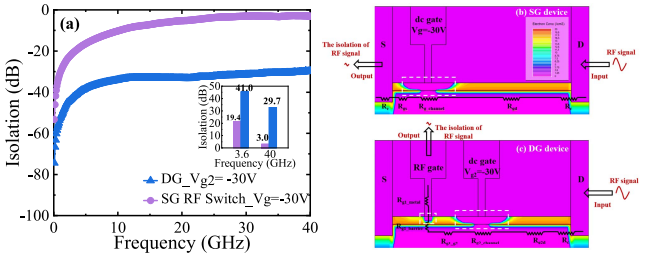

FIGURE 10. **(a) Comparison of RF switch performance between SG RF switch and DG device. The electron concentration distribution and the resistance scheme of signal transmission path for (b) SG RF switch device and (c) DG integrated device.**

reason is that DG device can significantly inhibit the peak electric field and reduce RF gate leakage current under high drain voltage, which can be seen in Fig. 7. The output power and PAE of AlGaN/GaN HEMTs are still limited by current collapse. Especially under high drain voltage, the current collapse will worsen more obviously. However, compared with SG devices, DG devices can significantly improve current collapse, as can be seen in Fig. 5.

Fig. 10(a) shows the comparison of the isolation performance of the SG RF switch device and DG integrated device. The isolation measurements of both devices were performed by Keysight E8363B network analyzer. In the Rx mode, the dc gate of SG and DG device were biased at −30V (which is lower than the threshold voltage). At the frequency of 3.6 GHz and 40 GHz, the isolation of the SG RF switch device achieves 19.4dB and 3.0 dB, respectively, while the DG integrated device reaches 41.0 dB and 29.7dB, respectively. Fig. 10 (b) and Fig. 10(c) presented the simulated electron concentration distribution and the resistance scheme of transmission path for SG and DG device. As shown in Fig. 10(b), for SG RF switch device, the depletion region under the gate switched off the signal transmission path from drain to source. As shown in Fig. 10(c), for DG device, the depletion region under the dc gate and RF gate barrier had the main effect on the isolation of signal transmission from drain to RF gate. Compared with SG device, RF gate in DG device provided additional depletion region. Compared with the SG RF switch device, due to the influence of the Schottky barrier depletion of the RF gate, the isolation of the DG integrated device is improved by 21.6 dB (at 3.6 GHz) and 26.7 dB (at 40 GHz).

Parameters of the three devices compared in this work are summarized in Table 1. In Tx mode, DG device can improve the output power density and power added efficiency of PA. In Rx mode, DG device can improve the isolation of RF switch. The GaN-based integrated device meets the performance requirements of PA and RF switch while the area of GaN-based integrated device is reduced by 34% compared with the area of the combination of one SG PA device and one SG RF switch. It is shown that the DG device provides a new type of solution for the integration of RF frontends.

TABLE 1. **Summary of key device parameters.**

Parameter	SG device Power Amplifier	SG device RF switch device	**DG device Integrated device**
L_g (μm)	0.5	0.5	**0.5**
W (μm)	200	200	**200**
L_{sd} (μm)	6	6	**6**
L_{sg} (μm)	1.4	1.4	**-**
L_{gd} (μm)	1.4	1.4	**-**
L_{sg1} (μm)	-	-	**1.4**
$L_{g1\text{-}g2}$ (μm)	-	-	**2.0**
L_{g2d} (μm)	-	-	**1.6**
f_T (GHz)	15.1	-	**14.6**
f_{MAX} (GHz)	36.4	-	**36.6**
I_{DQ} (mA)	21.72	-	**19.48**
V_{DQ} (V)	50	-	**50**
PAE (%)	44.3	-	**51.1**
P_{out} (W/mm)	6.90	-	**7.85**
Gain (dB)	18.7	-	**17.9**
ISO (dB)	-	19.4dB(3.6GHz) 3.0dB(40GHz)	**41.0dB(3.6GHz) 29.7dB(40GHz)**
Area (mm^2)	0.20	0.18	**0.25**
	0.38 (One SG PA device and one SG RF Switch device)		

TABLE 2. **Comparison of PA performance with other literatures.**

Year	Organization	V_{DQ}	P_{out}	PAE	Data Sources
2016	HRL	28V	2.5 W/mm	70%	[20]
2009	UCSB	20V	4.1 W/mm	71%	[30]
2011	Mitsubishi	40V	10 W/mm	62%	[31]
2011	XD University	45V	13.3 W/mm	73%	[11]
2014	Cree	28V	4.9 W/mm	60%	[32]
2016	TriQuint	50V	6.3 W/mm	70%	[33]
2019	Qorvo	32V	5.37W/mm	65.5%	[34]
2020	Wolfspeed	50V	7.6W/mm	65%	[35]
2023	XD University	50V	7.85W/mm	51.1%	This work

TABLE 3. **Comparison of isolation with other literatures.**

Organization	**Frequency range**	**Isolation**	**Data Source**
IAF	28-51 GHz	23.5-27 dB	[36]
University of Rome Tovergata	33-39 GHz	22 dB	[37]
Beijing Institute of Technology University	30-40 GHz	25 dB	[38]
Qorvo	40 GHz	25.63 dB	[39]
Raytheon	27-31 GHz	25 dB	[40]
University of Electronic Science and Technology of China	32-38 GHz	20	[41]
Results above were measured from SPDT.			
XD University	**40 GHz**	**29.7 dB**	**This work**
Results above were measured from RF switch device.			

Table 2 compared the PA performance of DG devices in this work and other literatures. The output power density of DG devices was comparable with some commercial results [33], [35]. In the future work, the PA performance of DG device can be further increased by reducing the ohmic contact resistance [5], [29] and optimizing epitaxial structure [42].

Table 3 benchmarks the isolation of single-pole double-throw circuit (SPDT) in other literatures and DG devices in this work at Ka band. As shown in Table 3, the isolation of DG devices is competitive with other SPDT results at Ka band.

IV. CONCLUSION

This paper presents dual-mode working principle based on GaN dual-gate device that integrates PA and RF switch In the Tx mode, DG device works as PA. The current collapse decreased to 6.4% for DG device, while the current collapse for SG device is 12.7%. At 3.6 GHz, the DG device achieved the peak PAE of 51.1% and the output power density of 7.85 W/mm, showing the improvement of power characteristics compared with SG device. In the Rx mode, the DG device works as RF switch and can achieve high isolation of 41.0 dB and 29.7 dB at frequency of 3.6 GHz and 40 GHz, respectively. Compared with the conventional RF switch device, the isolation of the integrated device is improved by 21.6 dB (3.6 GHz) and 26.7 dB (40 GHz), respectively. The area of DG devices is reduced by 34% compared with the area of the combination of one SG PA device and one SG RF switch. These results indicate that the GaN dual-gate device could be a promising technique for RF frontends applications.

REFERENCES

[1] A. Bettidi et al., "Innovative T/R module in state-of-the-art GaN technology," in *Proc. Radar Conf.*, 2008, pp. 1–5, doi: 10.1109/RADAR.2008.4720975.

[2] P. Schuh et al., "GaN MMIC based T/R-module front-end for X-band applications," in *Proc. EMICC*, 2008, pp. 274–277, doi: 10.1109/EMICC.2008.4772282.

[3] C. An and H.-G. Ryu, "MIMO receiver system using single RF front-end," in *Proc. Int. Conf. SPIN*, 2014, pp. 297–300, doi: 10.1109/SPIN.2014.6776966.

[4] K. Harrouche, R. Kabouche, E. Okada, and F. Medjdoub, "High performance and highly robust AlN/gan HEMTs for millimeter-wave operation," *IEEE J. Electron Devices Soc.*, vol. 7, pp. 1145–1150, 2019, doi: 10.1109/JEDS.2019.2952314.

[5] J. S. Moon et al., "55% PAE and high power Ka-band GaN HEMTs with linearized transconductance via n+ GaN source contact ledge," *IEEE Electron Device Lett.*, vol. 29, no. 8, pp. 834–837, Aug. 2008, doi: 10.1109/LED.2008.2000792.

[6] C. Lee, P. Saunier, J. Yang, and M. A. Khan, "AlGaN-GaN HEMTs on SiC with CW power performance of >4 W/mm and 23% PAE at 35 GHz," *IEEE Electron Device Lett.*, vol. 24, no. 10, pp. 616–618, Oct. 2003, doi: 10.1109/LED.2003.817383.

[7] A. Koudymov et al., "Low-loss high power RF switching using multi-finger AlGaN/GaN MOSHFETs," *IEEE Electron Device Lett.*, vol. 23, no. 8, pp. 449–451, Aug. 2002, doi: 10.1109/LED.2002.801301.

[8] H. Ishida et al., "A high-power RF switch IC using AlGaN/GaN HFETs with single-stage configuration," *IEEE Trans. Electron Devices*, vol. 52, no. 8, pp. 1893–1899, Aug. 2005, doi: 10.1109/TED.2005.851835.

[9] G. Simin et al., "Multigate GaN RF switches with capacitively coupled contacts," *IEEE Electron Device Lett.*, vol. 30, no. 9, pp. 895–897, Sep. 2009, doi: 10.1109/LED.2009.2025675.

[10] U. K. Mishra, P. Parikh, and Y.-F. Wu, "AlGaN/GaN HEMTs-an overview of device operation and applications," *Proc. IEEE*, vol. 90, no. 6, pp. 1022–1031, Jun. 2002, doi: 10.1109/JPROC.2002.1021567.

[11] Y. Hao et al., "High-performance microwave gate-recessed AlGaN/AlN/GaN MOS-HEMT with 73% power-added efficiency," *IEEE Electron Device Lett.*, vol. 32, no. 5, pp. 626–628, May 2011, doi: 10.1109/LED.2011.2118736.

[12] H. Lu et al., "Improved RF power performance of AlGaN/GaN HEMT using by Ti/Au/Al/Ni/Au shallow trench etching ohmic contact," *IEEE Trans. Electron Devices*, vol. 68, no. 10, pp. 4842–4846, Oct. 2021, doi: 10.1109/TED.2021.3101462.

[13] R. S. Pengelly, S. M. Wood, J. W. Milligan, S. T. Sheppard, and W. L. Pribble, "A review of GaN on SiC high electron-mobility power transistors and MMICs," *IEEE Trans. Microw. Theory Techn.*, vol. 60, no. 6, pp. 1764–1783, Jun. 2012, doi: 10.1109/TMTT.2012.2187535.

[14] F. Medjdoub, N. Herbecq, A. Linge, and M. Zegaoui, "High frequency high breakdown voltage GaN transistors," in *IEDM Tech. Dig.*, 2015, pp. 9.2.1–9.2.4, doi: 10.1109/IEDM.2015.7409660.

[15] M. Wu et al., "First demonstration of state-of-the-art GaN HEMTs for power and RF applications on a unified platform with free-standing GaN substrate and Fe/C Co-doped buffer," in *Proc. Int. Electron Devices Meet. (IEDM)*, San Francisco, CA, USA, 2022, pp. 11.3.1–11.3.4, doi: 10.1109/IEDM45625.2022.10019550.

[16] H. Lu et al., "High RF performance GaN-on-Si HEMTs with passivation implanted termination," *IEEE Electron Device Lett.*, vol. 43, no. 2, pp. 188–191, Feb. 2022, doi: 10.1109/LED.2021.3135703.

[17] L. Yang et al., "Investigation on the influence of ohmic structure on channel-to-channel coupling effect in InAlN/GaN double channel HEMTs," *IEEE J. Electron Devices Soc.*, vol. 10, pp. 474–480, 2022, doi: 10.1109/JEDS.2022.3183638.

[18] S. Osmanoglu and E. Ozbay, "X-band high power GaN SPDT MMIC RF switches," in *Proc. Eur. Microw. Conf. Cent. Eur.*, 2019, pp. 83–86.

[19] F. Thome and O. Ambacher, "Highly isolating and broadband single-pole double-throw switches for millimeter-wave applications up to 330 GHz," *IEEE Trans. Microw.Theory Tech.*, vol. 66, no. 4, pp. 1998–2009, Apr. 2018, doi: 10.1109/TMTT.2017.2777980.

[20] J. S. Moon et al., ">70% Power-added-efficiency dual-gate, cascode GaN HEMTs without harmonic tuning," *IEEE Electron Device Lett.*, vol. 37, no. 3, pp. 272–275, Mar. 2016, doi: 10.1109/LED.2016.2520488.

[21] S.-E. Shih et al., "Design and analysis of ultra wideband GaN dual-gate HEMT low-noise amplifiers," *IEEE Trans. Microw. Theory Tech.*, vol. 57, no. 12, pp. 3270–3277, Dec. 2009, doi: 10.1109/TMTT.2009.2034416.

[22] L. Yang et al., "Improvement of subthreshold characteristic of gate-recessed AlGaN/GaN transistors by using dual-gate structure," *IEEE Trans. Electron Devices*, vol. 64, no. 10, pp. 4057–4064, Oct. 2017, doi: 10.1109/TED.2017.2741001.

[23] M. Meneghini et al., "Buffer traps in Fe-doped AlGaN/GaN HEMTs: Investigation of the physical properties based on pulsed and transient measurements," *IEEE Trans. Electron Devices*, vol. 61, no. 12, pp. 4070–4077, Dec. 2014, doi: 10.1109/TED.2014.2364855.

[24] M. T. Hasan, T. Asano, H. Tokuda, and M. Kuzuhara, "Current collapse suppression by gate field-plate in AlGaN/GaN HEMTs," *IEEE Electron Device Lett.*, vol. 34, no. 11, pp. 1379–1381, Nov. 2013, doi: 10.1109/LED.2013.2280712.

[25] Y. Zhou et al., "High efficiency over 70% at 3.6-GHz InAlN/GaN HEMT fabricated by gate recess and oxidation process for low-voltage RF applications," *IEEE Trans. Electron Devices*, vol. 70, no. 1, pp. 43–47, Jan. 2023, doi: 10.1109/TED.2022.3225762.

[26] R. Vetury, N. Q. Zhang, S. Keller, and U. K. Mishra, "The impact of surface states on the DC and RF characteristics of AlGaN/GaN HFETs," *IEEE Trans. Electron Devices*, vol. 48, no. 3, pp. 560–566, Mar. 2001, doi: 10.1109/16.906451.

[27] S. Ghosh et al., "OFF-state leakage and current collapse in AlGaN/GaN HEMTs: A virtual gate induced by dislocations," *IEEE Trans. Electron Devices*, vol. 65, no. 4, pp. 1333–1339, Apr. 2018, doi: 10.1109/TED.2018.2808334.

[28] M. Mi et al., "Millimeter-wave power AlGaN/GaN HEMT using surface plasma treatment of access region," *IEEE Trans. Electron Devices*, vol. 64, no. 12, pp. 4875–4881, Dec. 2017, doi: 10.1109/TED.2017.2761766.

[29] Y. Lu et al., "High RF performance AlGaN/GaN HEMT fabricated by recess-arrayed ohmic contact technology," *IEEE Electron Device Lett.*, vol. 39, no. 6, pp. 811–814, Jun. 2018, doi: 10.1109/LED.2018.2828860.

[30] M. H. Wong, Y. Pei, D. F. Brown, S. Keller, J. S. Speck, and U. K. Mishra, "High-performance N-face GaN microwave MIS-HEMTs with > 70% power-added efficiency," *IEEE Electron Device Lett.*, vol. 30, no. 8, pp. 802–804, Aug. 2009, doi: 10.1109/LED.2009.2024443.

[31] K. Yamanaka, M. Kimura, S. Chaki, M. Nakayama, and Y. Hirano, "S-band internally harmonic matched GaN FET with 330W output power and 62% PAE," in *Proc. 6th Eur. Microw. Integr. Circuit Conf.*, 2011, pp. 244–247.

[32] "CGH40035: 35 W, DC - 4 GHz, RF Power GaN HEMT." Accessed: 2020. [Online]. Available: https://assets.wolfspeed.com/uploads/2020/12/CGH40035.pdf, EB page
[33] "QPD1010: DC - 4 GHz, 10 watt, 50 volt GaN RF transistor," 2021. [Online]. Available: https://cn.qorvo.com/products/p/QPD1010#documents, WEB page
[34] "TGF2023-2-10: DC - 14 GHz, 50 Watt Discrete Power GaN on SiC HEMT." 2023. [Online]. Available: https://cn.qorvo.com/products/p/TGF2023-2-10 #documents, WEB,page
[35] "CGHV40320D: 320-W 4.0-GHz, GaN HEMT Die." Accessed: 2020. [Online]. Available: https://assets.wolfspeed.com/uploads/2020/12/ CGHV40320D.pdf, WEB page
[36] F. Thome, P. Brückner, R. Quay, and O. Ambacher, "Millimeter-wave single-pole double-throw switches based on a 100-nm gate-length AlGaN/GaN-HEMT technology," in *Proc. IEEE MTT-S Int. Microw. Symp. (IMS)*, Boston, MA, USA, 2019, pp. 1403–1406, doi: 10.1109/MWSYM.2019.8700955.
[37] G. Polli et al., "GaN/Si Ka-band SPDT for observation payloads," in *Proc. IEEE Asia-Pac. Microw. Conf. (APMC)*, Singapore, 2019, pp. 288–290, doi: 10.1109/APMC46564.2019.9038632.
[38] D. Guo, T. Qiao, X. Luo, and M. Li, "Design of a Ka-band broadband SPDT switch MMIC based on GaN HEMTs," in *Proc. IEEE 16th Int. Conf. Commun. Technol. (ICCT)*, Hangzhou, China, 2015, pp. 241–243, doi: 10.1109/ICCT.2015.7399832.
[39] "TGS4302: 27 - 46 GHz Ka band high power SPDT switch," 2021. https://cn.qorvo.com/products/p/TGS4302#documents, Web Page
[40] X. Zheng, J. C. Tremblay, S. E. Huettner, K. P. Ip, T. Papale, and K. L. Lange, "Ka-band high power GaN SPDT switch MMIC," in *Proc. IEEE Compound Semicond. Integr. Circuit Symp. (CSICS)*, Monterey, CA, USA, 2013, pp. 1–5, doi: 10.1109/CSICS.2013.6659234.
[41] L. Wang, Y. Fan, and Y. J. Cheng, "Design of low loss Ka-band SPDT switch based on AlGaN/GaN HEMT technology," in *Proc. IEEE MTT-S Int. Microw. Workshop Series Adv. Mater. Process. RF THz Appl. (IMWS-AMP)*, Guangzhou, China, 2022, pp. 1–3, doi: 10.1109/IMWS-AMP54652.2022.10107090.
[42] F. Jia et al., "The influence of fe doping tail in unintentionally doped GaN layer on DC and RF performance of AlGaN/GaN HEMTs," *IEEE Trans. Electron Devices*, vol. 68, no. 12, pp. 6069–6075, Dec. 2021, doi: 10.1109/TED.2021.3123113.